International Journal of Solids and Structures 212 (2021) 80–94

Contents lists available at ScienceDirect

International Journal of Solids and Structures

journal homepage: www.elsevier.com/locate/ijsolstr

# Fracture behavior of additively printed ABS: Effects of print architecture and loading rate

John P. Isaac, Sivareddy Dondeti, Hareesh V. Tippur *

*Department of Mechanical Engineering, Auburn University, AL 36849, United States*

ARTICLE INFO

*Article history:*
Received 17 May 2020
Received in revised form 5 October 2020
Accepted 21 November 2020
Available online 30 November 2020

*Keywords:*
Additive manufacturing
Build architecture
Fracture mechanics
Crack growth resistance
Strain-rate effects
Digital image correlation

ABSTRACT

Acrylonitrile Butadiene Styrene (ABS) is an inexpensive amorphous thermoplastic used for Additive Manufacturing (AM) of engineering parts. Fused Filament Fabrication (FFF) is commonly used to 3D print ABS, and it involves layer-by-layer deposition of melted thermoplastic wire through a heated nozzle along predetermined paths. The individual layers can also be configured differently and could introduce mechanical anisotropy into the final part in terms of weak planes between individual beads and layers even when the feedstock is isotropic. In this context, this research examines the dynamic fracture behaviors of three different print architectures, namely $[0°/90°]_n$, $[45°/-45°]_n$ and $[0°/45°/90°/-45°]_n$ in-plane orientations, under stress-wave loading conditions and compares the results with the quasi-static counterparts. The dynamic experiments are carried out using a modified-Hopkinson pressure bar apparatus. The full-field measurement of in-plane displacements are performed using Digital Image Correlation (DIC) and ultrahigh-speed photography of V-notched specimens subjected to stress-wave loading. A novel method of analyzing DIC data by transferring it to a finite element environment to compute the *J*-integral using prevailing domain integral algorithms is introduced. Distinct crack initiation and growth behaviors with different failure modes are observed in the three architectures under static and dynamic loading conditions despite the macroscale elastic isotropy. The results favor $[0°/45°/90°/-45°]_n$ architecture due to a better crack growth behavior relative to the other two, raising the possibility of fracture performance enhancement by tailoring the build architecture.



## 1. Introduction

Additive Manufacturing (AM) has become popular for producing engineering parts made of plastics, metals, and ceramics by building objects layer-by-layer (Terminology, 2012). Its ability to produce complex shapes on demand and in limited quantities has made AM desirable in biomedical, automotive and aerospace industries alike. Fused Filament Fabrication (FFF) is one of the many types of AM processes used to print thermoplastics (Mohamed et al., 2015) extensively. Because of the low melting point, thermoplastics such as PLA, ABS, PET, PA, and PVA are often used for FFF. These thermoplastics available as spools of filament/wire stock are melted and deposited by a heated nozzle layer-by-layer on a heated bed in computer-generated patterns (Bourell et al., 2014). This layer-by-layer printing process, however, introduces artifacts affecting their mechanical failure characteristics and hence needs to be investigated when parts are to meet critical functionality. That is, prescribing the path of the nozzle introduces weaker planes in the resulting AM parts (Ahn et al., 2002) and hence, the role the build/print architecture needs to be studied and understood (Al-Maharma and Sendur, 2018). The loading rate could add to this complexity further if the base material is strain-rate dependent (Mulliken and Boyce, 2006; Siviour and Jordan, 2016; Walley and Field, 1994). Thus parts made by FFF might behave differently under high strain-rate conditions and need attention as well.

ABS has applications (Van de Velde and Kiekens, 2002; Poh et al., 2016) in biomedical (implants, prosthetics), furniture and fashion (shoes, watches), and aviation and automotive industries (fuel injectors). Because of its bio-compatibility and compliancy, ABS is one of the popular amorphous thermoplastics used for FFF or FDM (Dizon et al., 2018). Accordingly, there are several reports on the mechanical behavior of AM parts. The effects of build direction and raster orientation on mechanical failure were studied in (Riddick et al., 2016) by performing quasi-static tension tests. The differences between the prints were explained using fractographic analyses to emphasize the significance of print architecture on mechanical strength. Enhancement of fracture properties

* Corresponding author.
*E-mail address:* htippur@eng.auburn.edu (H.V. Tippur).

https://doi.org/10.1016/j.ijsolstr.2020.11.027
0020-7683/

of AM parts by printing along paths based on the knowledge of stresses acting on the component was demonstrated in (Gardan et al., 2016). The fracture toughness was found to increase in additively printed ABS samples under mixed-mode loading conditions when the deposition path was along the principal stress directions (Lanzillotti et al., 2019). Some studies have also shown that infill pattern and the build direction with respect to the pre-crack affects the failure parameters (Papon and Haque, 2019; Jia and Wang, 2019; Mclouth et al., 2017; Aliheidari et al., 2017). In terms of fracture properties, layer and build orientations and infill percentages were found to be the main factors controlling the fracture toughness of AM parts produced through FFF process (Young et al., 2018; Rabbi et al., 2019; Samykano et al., 2019; Hart and Wetzel, 2017). The effect of strain-rate on the tensile strength of ABS manufactured via AM was studied in (Vairis et al., 2016) and increased moduli and tensile strengths were observed at higher loading rates. Dynamic shear and fracture behavior of bulk ABS under dynamic loading was studied in (Lee and Shen, 2004) and increase in yield stress, shear modulus and stress softening amplitude were observed. A few other works have studied strain-rate sensitivity of fracture properties of ABS AM parts under dynamic loading conditions, and variation in crack initiation toughness with respect to raster orientations was reported (Rabbi et al., 2019; Peterson and Bolling, 2015). Some previous works (Hart and Wetzel, 2017; Mclouth et al., 2017; Aliheidari et al., 2017; Young et al., 2018; Rabbi et al., 2019) have reported on the fracture behavior in terms of crack initiation, but they have relied on far-field load or deflection measurements to assess the performance. Some others (Jia and Wang, 2019; Peterson and Bolling, 2015) have utilized optical imaging to study the crack growth behavior but without performing any kinematic measurements. Thus, to our knowledge, no work has been reported on both the crack initiation *and* growth behaviors by quantifying the local mechanical fields to reveal the intricacies of the fracture behavior of 3D printed parts.

In this work, three different planar print architectures, namely $[0°/90°]_n$, $[\pm45°]_n$ and $[0°/45°/90°/-45°]_n$ are employed to evaluate the effect of print architecture and strain-rate sensitivity on tensile and the fracture properties of additively manufactured ABS coupons. Digital Image Correlation (DIC) (Pan et al., 2009) is employed for quantitative visualization. In many previous studies on conventional structural materials, the measured displacements obtained from DIC are used in conjunction with the theoretical expressions and over-deterministic least-squares error minimization approach to determine the crack tip fracture parameters such as Stress Intensity Factors (SIF) (Yoneyama et al., 2007; Lee et al., 2009; Kirugulige and Tippur, 2009). In this work, a novel approach of transferring experimentally measured displacements obtained from DIC to customized Finite Element (FE) discretization for extracting the energy release rate (the *J*-integral) using proven algorithms available in Abaqus, Ansys, etc. A few previous works (Barhli et al., 2017; Pitti et al., 2014; Becker et al., 2012, 2011; Hareesh and Chiang, 1988) have carried out such calculations but on *traditional materials* by applying optically measured displacements as boundary conditions for FE sub-models. In this work, however, the geometry of the specimen surface in the Region-of-Interest (ROI) recorded by the camera is modeled as a FE mesh in Abaqus by matching the DIC grid. The measured displacements are then imported into the discretized model as full-field surface boundary conditions. Subsequently, the in-built modules in Abaqus are employed for extracting the fracture parameters.

In the following, details about specimen fabrication including information regarding the three different print architectures studied are described first. The tension tests, quasi-static fracture tests, ultrasonic wave-speed measurements and dynamic fracture tests are described in the subsequent sections. Then, a detailed explanation of the methodology of extracting the *J*-Integral values is included before presenting the results pertaining to the role of print architecture and loading rate effects on the tensile and fracture behaviors of AM printed ABS. It is then followed by discussion of results before presenting the major conclusions.

## 2. Specimen fabrication

A Cubicon 3DP-110F printer was used to print all specimens studied in this work. The desired geometry was modeled using Solidworks® and exported to the slicer software as a stereolithographic (.STL) file. All print settings and modifications were finalized using the slicer software and a G-code was generated and exported to the printer. Three planar architectures namely, $[0°/90°]_n$, $[45°/-45°]_n$ and $[0°/45°/90°/-45°]_n$ were printed with identical printer parameters listed in Table 1. A 100% infill option was selected for all three architectures to obtain fully dense specimens and to avoid effects of any additional porosity besides the one inherent to the printing process itself. $[0°/90°]_n$ and $[45°/-45°]_n$ are default architectures in most 3D printers and the rationale for these architectures from the mechanical performance perspective is mostly intuitive. Therefore, for starters, the $[0°/45°/90°/-45°]_n$ architecture was chosen besides the $[0°/90°]_n$ and $[45°/-45°]_n$ to demonstrate that there could be other raster patterns among the infinite number of possibilities for achieving improved mechanical performance.

During printing, the outer wall was first deposited in each layer of the specimen and then the printer nozzle was moved in directions specific to the above three patterns in the *x*-*y* plane. A schematic of the layer buildup (in the *z*-direction) used for the three architectures are shown in Fig. 1. That is, in $[0°/90°]_n$ architecture, the nozzle moved parallel to the *x*-axis for the first layer and perpendicular to the *x*-axis in the second layer, and so on. Within each layer, the nozzle followed a serpentine path to achieve 100% fill. This alternating bilayer buildup was continued until the desired thickness was achieved in the *z*-direction. Similarly, in the $[45°/-45°]_n$ architecture, the first layer was at 45° to the *x*-axis and the second layer was at −45° or 135° to the *x*-axis. In the $[0°/45°/90°/-45°]_n$ architecture, on the other hand, a repeating four layer buildup of a combination of the two preceding architectures, was implemented. That is, the first layer was along 0°, the second was along 45°, the third was along 90° and the fourth was along −45° to the *x*-axis. The subsequent layers were repeated thereafter. Although ABS is a nominally isotropic material, because of the different paths followed by the deposition nozzle during printing, anisotropy in terms of weak planes were expected in the printed specimens. *From here onwards, for simplicity of description,* $[0°/90°]_n$, $[45°/-45°]_n$ *and* $[0°/45°/90°/-45°]_n$ *architectures will be named as* A1, A2 *and* A3, *respectively.* Note that the number of layers *n* (typically 25–30) in a printed specimen depends on the constant layer thickness of 0.2 mm used during printing.

## 3. Experimental details

### 3.1. Tension tests

First, uniaxial tension tests were carried out on all three print architectures A1, A2 and A3, described earlier. An Instron 4465

**Table 1**
3D printer parameters.

| Print parameters | Values | Print parameters | Values |
|---|---|---|---|
| Extruder temperature | 240 °C | Layer thickness | 0.2 mm |
| Bed temperature | 115 °C | Wall thickness | 0.8 mm |
| Chamber temperature | 50 °C | Infill speed | 80 mm/s |
| Nozzle flow Percentage | 100% | Nozzle retraction speed | 40 mm/s |

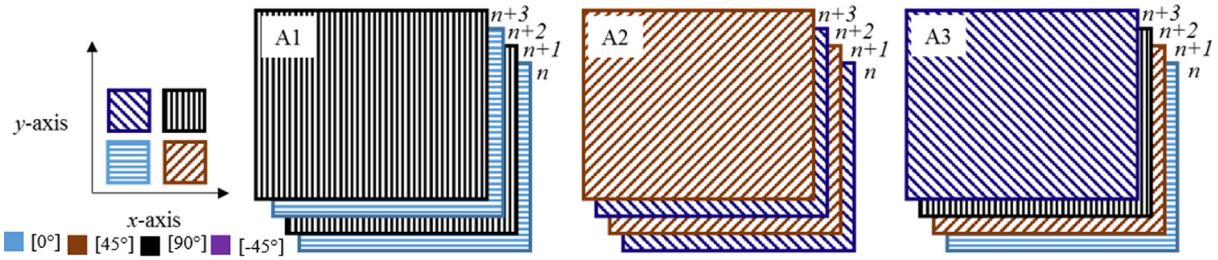


**Fig. 1.** Build direction of each layer of print architectures designated A1, A2 and A3. A serpentine pattern was adopted during printing of each layer of the architecture. The hatch marks in each layer correspond to 0°, 45°, 90°, −45° directions.

mechanical tester fitted with a 5 kN load-cell was used to carry out tests on dog-bone shaped specimens of 8 mm width and 4 mm thickness in the gage section. Fig. 2(a) shows the dimensions of the specimen used. They were sprayed with mists of black and white paint to create random speckles on one of the surfaces to perform 2D-DIC in the gage section and measure in-plane deformations. A PointGrey monochrome camera (2048 × 2048 pixels fitted with a 18–208 mm focal length macro zoom lens) recorded the event at a rate of 2 frames per second (fps) or 0.5 sec interval. The experiments were performed in the displacement control mode at a crosshead speed of 0.05 mm/s. During each test, time, load and crosshead displacement data were all recorded until the specimen failed.

### 3.2. Tension and shear tests on reference architectures

Uniaxial tension and pure shear tests were carried out next on two reference architectures with $[0°]_n$ and $[90°]_n$ raster. This included (a) separate uniaxial tension tests on plain $[0°]_n$ and $[90°]_n$ architectures, and (b) Iosipescu shear tests (O'Dowd et al., 1992) on $[0°]_n$ samples (Fig. 2(b)). In these reference architectures, all the layers over the entire build thickness in the *z*-direction of the sample were unidirectional but other specimen details were same as the ones used for A1, A2 and A3.

### 3.3. Quasi-static fracture tests

Fracture tests were carried out under quasi-static loading conditions on all three print architectures – A1, A2 and A3. Fig. 2(c) shows dimensions of edge-notched symmetric three-point bend specimens. A 6 mm long notch was inserted into the specimen edge using a 300 μm thick circular saw at the mid-span and its root was sharpened by scoring the notch-front with a razor blade to achieve a sharp starter crack (Fig. 2(c). Again, an Instron 4465 mechanical tester with a 5 kN load cell, equipped with a roller loading pin of diameter 12.7 mm, was used to carry out these experiments at a crosshead speed of 0.007 mm/s and time, load, and crosshead displacement histories were all recorded during each test. As in the tension tests, a fine coat of random speckles was sprayed on one of the faces of the specimen in order to per-

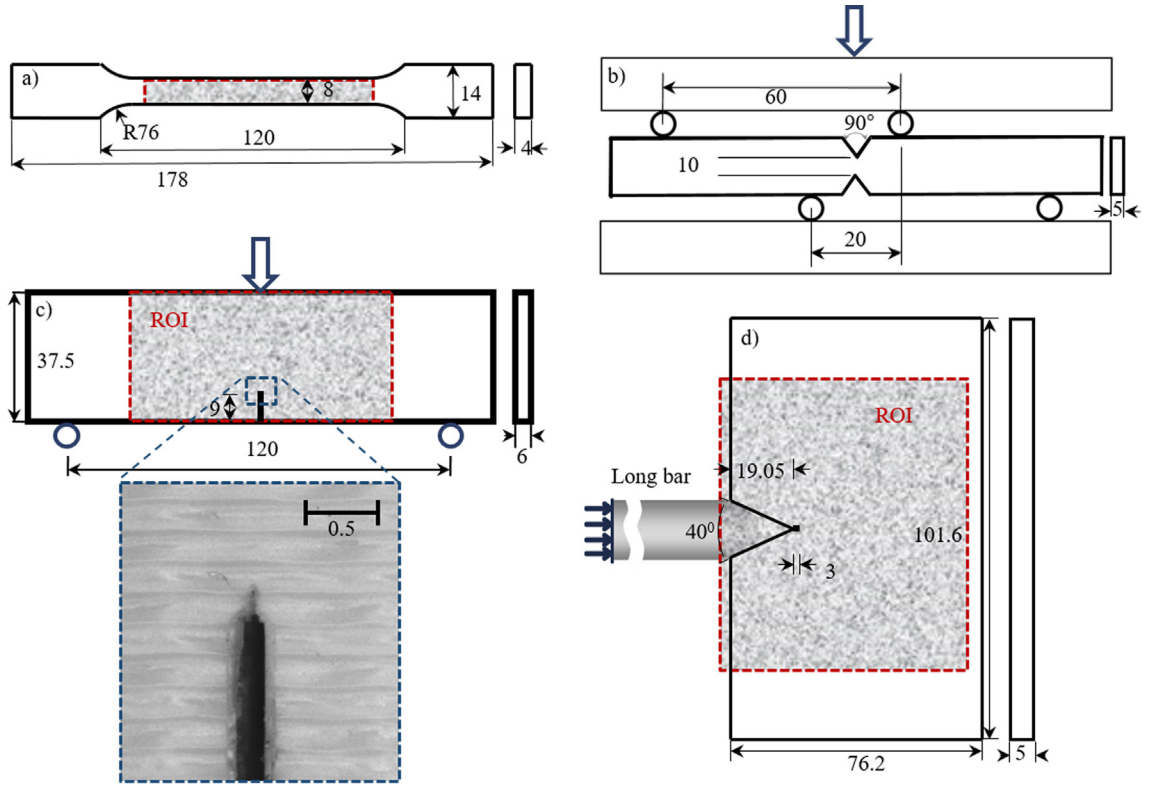


**Fig. 2.** (a) Tension specimen geometry. (b) Iosipescu shear tests specimen geometry and loading configuration. (c) Quasi-static fracture specimen loading and geometry with an inset of the crack tip sharpened by a razor blade. (d) Dynamic fracture specimen loading and geometry. (*All dimensions are in mm*).

form DIC and quantify in-plane displacements. Again, the Point-Grey camera was used to record the speckle images at 2 fps during tests. As in the tension tests, specimens of all three architectures were tested until crack initiation and significant growth occurred.

### 3.4. Ultrasonic measurements

Ultrasonic measurements were performed on 12.7 mm cubes printed in A1, A2 and A3 architectures. An ultrasonic tester, Olympus Epoch 600, was used for launching elastic waves into the specimen in all three directions and in all three print architectures. The elastic wave speeds for both longitudinal and shear waves were recorded along all the three axes of rotation. A schematic of the setup used in these measurements is shown in Fig. 3. The longitudinal (2.25 MHz) ($C_L$) and shear (5 MHz) ($C_S$) wave transducers were employed separately to measure the time-of-flight using which the respective wave speeds were determined. These values along with separately measured mass density (ρ)used in conjunction with Eq. (1) resulted in *dynamic* elastic constants, $E$ and ν, for each print architecture.

$$C_L = \sqrt{\frac{E(1-\nu)}{\rho(1+\nu)(1-2\nu)}}, \quad C_S = \sqrt{\frac{E}{2\rho(1+\nu)}} \tag{1}$$

### 3.5. Dynamic fracture tests

Impact induced fracture behavior of all the three print architectures was studied next. A modified Hopkinson pressure bar (or a long-bar) apparatus was used for loading the specimens using stress waves. An ultrahigh-speed camera was used to perform time-resolved 2D-DIC measurements around dynamically loaded cracks. Fig. 4 shows a schematic of the loading apparatus along with the arrangement for optical recording of speckles during the event. The aluminum 7075-T6 long-bar was approx. 1.8 m long (72 in.) and 25.4 mm (1 in.) in diameter and was held in place by a couple of pillow blocks. An aluminum striker rod of length 317.5 mm (12.5 in.) and diameter 25.4 mm (1 in.) was propelled from the barrel of a gas-gun to impact the long-bar and generate stress waves. The other end of the long-bar had a wedge profile and was in contact with the specimen having a 40° V-notch matching the loading tip of the long-bar. That is, the V-notch flanks of the specimen were pressed against the long-bar prior to the start of stress wave loading event. Fig. 2(d) shows the dimensions of the specimen; it had a 3 mm long straight notch inserted into the specimen at the apex of the V-notch using a 300 μm thick circular saw and the notch-tip was sharpened using a razor blade as in the static fracture experiments. The specimen was placed over a 100 mm long strip of soft putty of ~3 mm thickness on a translation stage with another identical strip pressed on to the top edge for achieving symmetry in terms of acoustic impedance relative to the loading axis. A Kirana-05 M ultrahigh-speed camera (924 × 768 pixels fitted with 70–300 mm focal length lens) was used to record dynamic deformations at a rate of 200,000 fps. In these experiments, a striker velocity of ~20 m/s was used for impact loading the specimens. A box padded with foam was used to catch the specimens after impact. The pillow blocks holding the long bar assisted in arresting the motion of the bar.

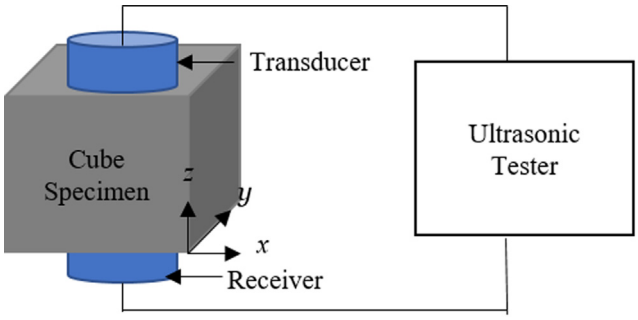


**Fig. 3.** Ultrasonic test setup.

## 4. Fracture parameter extraction

The 2D version of DIC method was used to measure two orthogonal in-plane displacement components on the specimen surface in the vicinity of the growing crack (Lee et al., 2009; Kirugulige and Tippur, 2009; Kirugulige et al., 2007). The displacements can be numerically differentiated to find the strain fields. Thus obtained strains from DIC are often noisy, particularly when deformations are small, say, in the elastic range. (To illustrate this, Fig. 5 shows experimentally measured displacements and the resulting normal strain fields obtained from DIC for a typical experiment on ABS, to be discussed subsequently.) Hence, the strains needed to calculate fracture parameters namely the path independent $J$-integral (Cherepanov, 1967; Rice, 1968);

$$J = \lim_{\Gamma \to 0} \int_{\Gamma} \left( W\delta_{1i} - \sigma_{ij} \frac{\partial u_j}{\partial x_1} \right) n_i \, dC, \quad (i,j = 1,2;\ x_1 = x,\ x_2 = y) \tag{2}$$

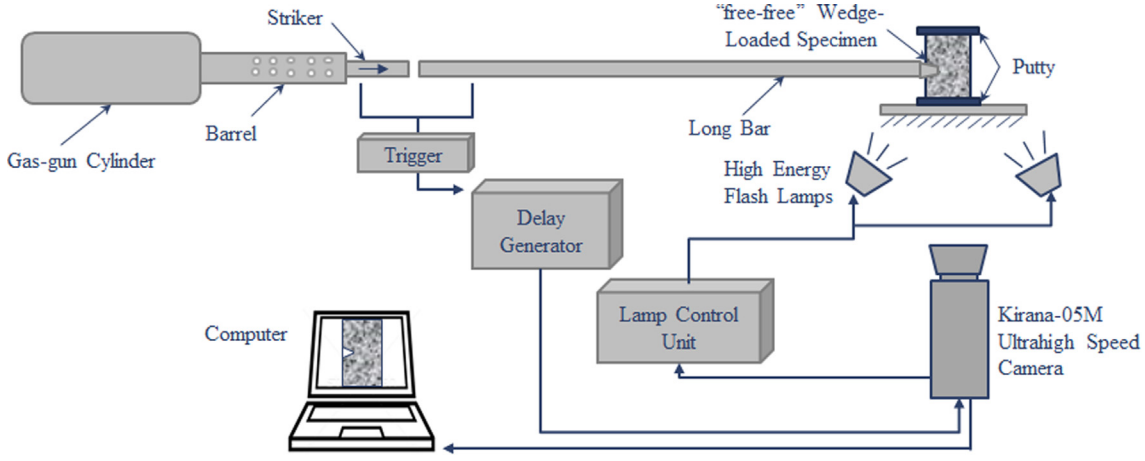


**Fig. 4.** Schematic of experimental setup used for dynamic fracture experiments.

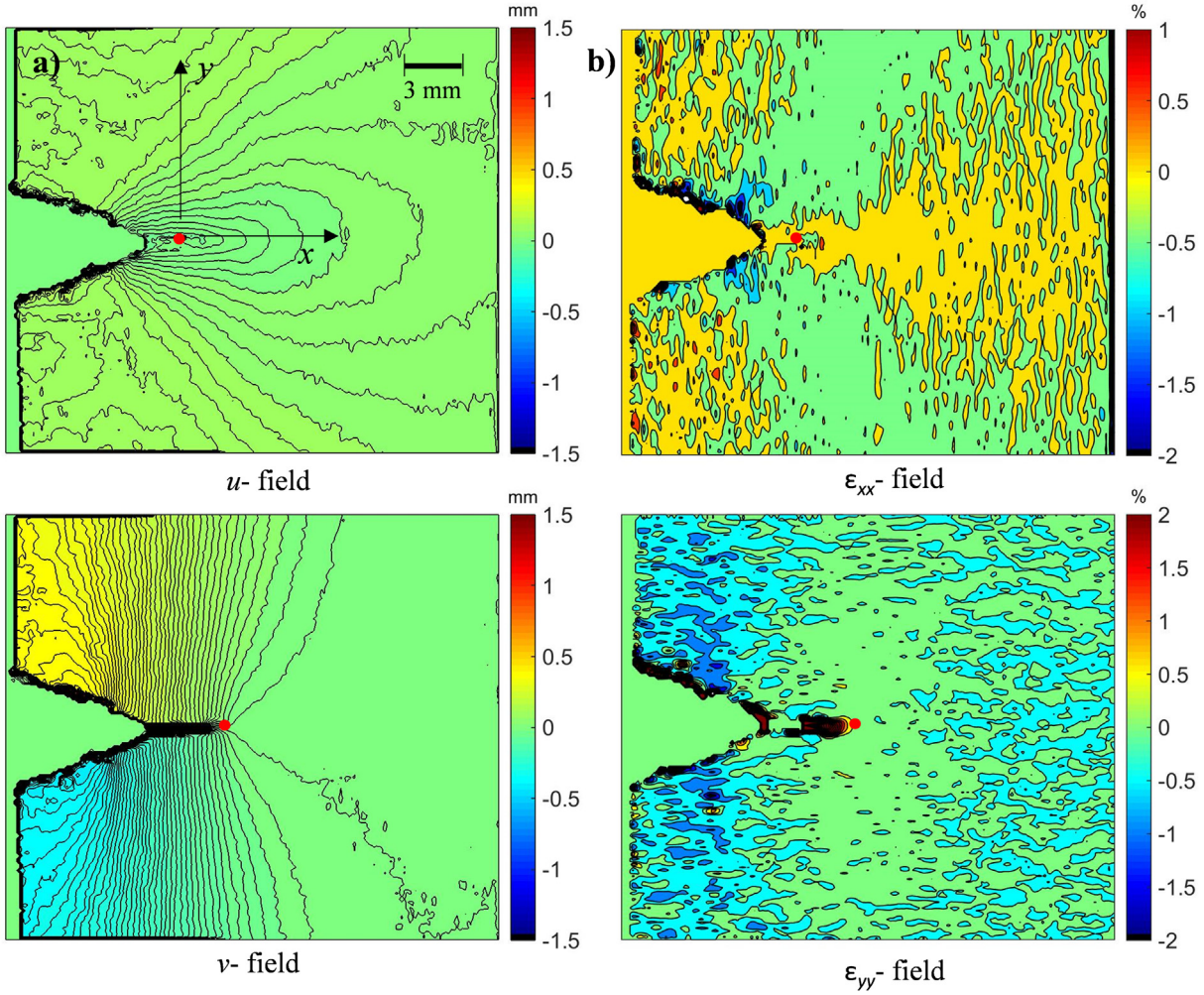


**Fig. 5.** Two orthogonal displacement fields, $u$ and $v$ in the $x$ and $y$-directions (a) and the corresponding normal strain fields (b) from DIC at a time instant/load step. A higher noise level in the strain field relative to the displacement fields is evident.

using standard *line integration* approach could be error prone without smoothing. In the above equation, $W$ is the strain energy density ($=\frac{1}{2}\sigma_{ij}\varepsilon_{ij}$), $\sigma_{ij}$ and $u_j$ are the Cartesian components of the stress ($\sigma_{11}=\sigma_{xx}$, $\sigma_{12}=\sigma_{xy}$, etc.) and displacements ($u_1=u$, $u_2=v$), $n_i$are components of the unit vector normal to the counterclockwise contour path $\Gamma$, $\delta_{1i}$ is the Kronecker delta and $dC$is the arc length along the contour. Being a path independent quantity, the $J$- integral can be a line, area or volume integral.

As noted in the literature review, the measured displacement fields can be analyzed directly by using them in conjunction with the prevailing elastic crack tip fields and over-deterministic least-squares analyses approaches (Kirugulige and Tippur, 2009; Kirugulige et al., 2007; Jajam and Tippur, 2011; Bedsole et al., 2015). Thus measured fracture parameters are generally sensitive to the number of terms of the asymptotic displacement field employed, the rigid body motions/rotations suffered by the specimen during loading, domain over which the data is extracted, crack tip triaxiality, etc. The results often are sensitive to the location of the crack tip. In light of these, a novel method of simply transferring the two measured orthogonal displacement data arrays from DIC into a 2D finite element model as surface (boundary) input to compute the energy release rate using robust *domain* (*area*) *integral* algorithms by defining the $J$-integral as,

$$J=\int_A\left(-W\delta_{1i}+\sigma_{ij}\frac{\partial u_j}{\partial x_1}\right)\frac{\partial q_1}{\partial x_1}\,dA,\quad (i,j=1,2), \tag{3}$$

is more attractive. In the above equation, $A$ is the area of the domain/ribbon of elements encircling the crack tip, $q_1$is a sufficiently smooth weighting function, and all others parameters are as defined previously. Hence, this new approach was adopted in this work as it eliminates most of the complexities that are associated with the traditional over-deterministic least-square analyses.

In DIC, the recorded images in the reference and deformed states are segmented into subsets/sub-images/facets of gray scales. Subsequently, the displaced location of a subset in the deformed state is determined relative to its undeformed state using a gray scale correlation algorithm. In doing so, each displacement data point in the full-field is an average value computed over the corresponding subset *at its center*. To implement the proposed approach, careful meshing was carried out in such a way that these displacement locations match the nodal locations in the finite element model consisting of a square grid of quad elements parallel and perpendicular to the specimen edges. It should be noted, however, that when the crack followed a kinked path[1] relative to its initial orientation, the neighborhood of the crack (region adjacent to the flanks) was discretized along a band using quad elements and the nodes were inputted with *interpolated* displacement boundary conditions from DIC subsets. It should be also noted that the crack tip

[1] When there was an increase in crack length with a change in its growth direction, FE models were updated with the new crack tip location; the new crack orientation was identified relative to the previous step.

was modeled simply as a sharp discontinuity since the *measured* displacements were used as 'input' to the FE model to *dictate* post-processing of DIC data to find the *J*-integral and then SIFs. Hence it should be noted that the sharpness of the crack tip in the model is unimportant; it is only the location and the orientation that matters.

A schematic of the steps followed is shown in Fig. 6. Experimentally measured displacement components from DIC were then imported as nodal 'boundary conditions' for the discretized field. The FE model was then run using Abaqus structural analysis software (v.16.1) after identifying the current crack tip position and its orientation to evaluate the fracture parameters using in-built algorithms.

The fracture parameters are reported by Abaqus for different contours. The first contour corresponds to the ring of elements encircling and embracing the crack tip and the second includes the first and the second rings, and so on. That is, as the contour number increases, the radial extent of the domain around the crack tip used for computing the *J*-integral increases. Since, the discretization corresponds to the sub-image overlap used while performing DIC (sub-image size = 25 pixels and sub-image overlap = 5 pixels, scale factor (optical magnification) ~0.06 mm/pixel), each additional ring corresponds to the radial increment equal to the sub-image overlap × the scale factor.

Fig. 7 shows an example of plot of the *J*-integral values, in terms of the contour numbers and radial distance from crack tip, at crack initiation for the A1 and A2 architectures. Evidently, the values do not show path independence in the very close vicinity of the crack tip (up to contour #10 or ~3 mm) due to a combined crack tip triaxial effects and inelastic deformations violating small scale yielding assumptions, and the finite size and shape functions of elements, among others. However, at larger distances of 3.6–13.5 mm (*r*/*B* ratio ~0.6–2.25, where *r* is the radial distance from crack tip and *B* is the specimen thickness) away from the crack tip, the values are rather stable and nearly constant (with ~5% variation). These stable values, averaged over contours 12–45 or 3.6 mm-13.5 mm (shaded region in Fig. 15), were recovered as the *J*-integral.

## 5. Results

### 5.1. Tension tests

The tensile stress-strain responses on two sets of specimens of all three architectures were measured. Results for one of the two sets are shown in Fig. 8. *Each specimen* type initially showed a linear response, up to approx. 1.5% engineering strain, and *essentially overlap on each other. This suggests that despite the differences in print architectures of* A1, A2 *and* A3*, they are all elastically identical* to within measurement errors. (Porosity was estimated from the failed specimen cross-sections for all three architectures and was approx. same at ~0.7%.) The elastic modulus was measured in each case using linear regression of data up to 0.1% strain. The sprayed-on random speckles were recorded to measure longitudinal and lateral strains in the gage section of the specimen using DIC to enable evaluation of the elastic constants $E$ and $\nu$ for each of the architectures. For brevity, a pair of representative strain fields from a uniaxial test on A1 architecture is shown in Appendix A. The strains from DIC were relatively uniform in the gage section, see Fig. A1(a). It also shows stress vs. axial and transverse strain plots (Fig. A1(b)) in the linear range for this architecture. These tension tests were repeatable for all three architectures. Two test results are shown for each of the architectures in Fig. A2(a) and good repeatability is self-evident.

The elastic modulus ($E$) and the Poisson's ratio ($\nu$) were found to be nearly same for all the three architectures and the difference in

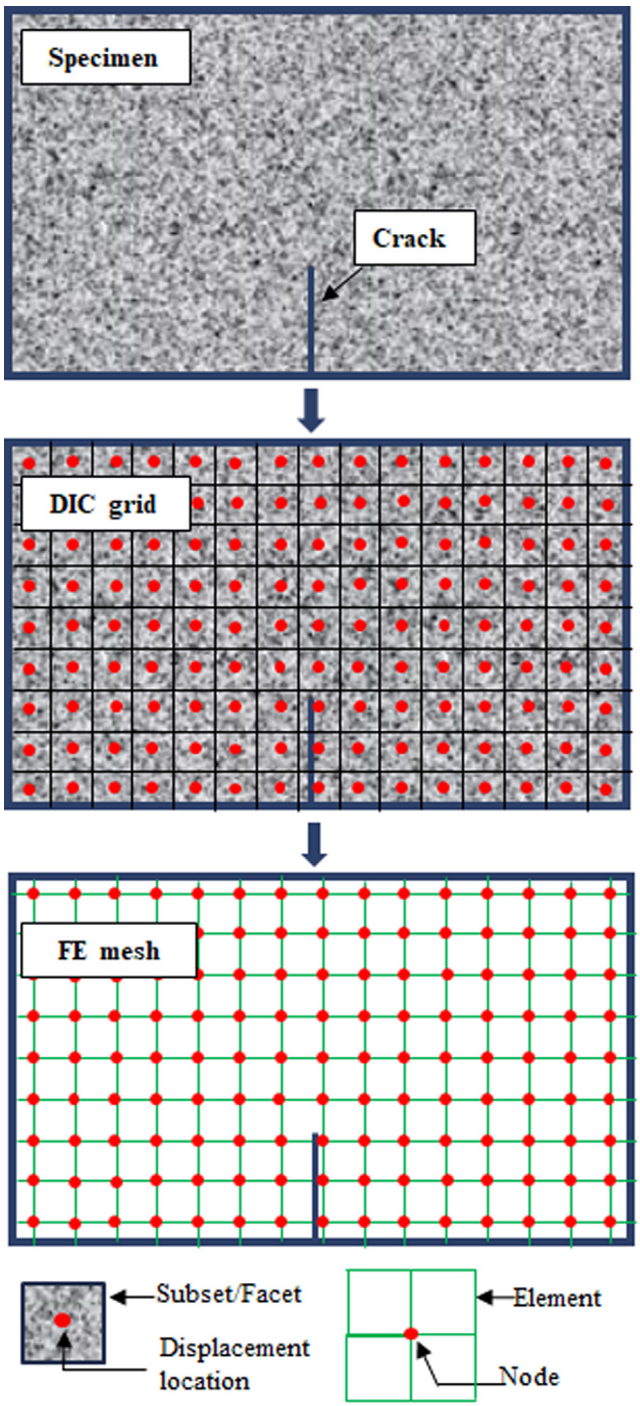


**Fig. 6.** The approach to compute the *J*-integral and SIFs by transferring DIC data into FE discretization for domain integration and mode-partitioning. The red dots are centers of sub-images and nodes of the FE grid. (For interpretation of the references to color in this figure legend, the reader is referred to the web version of this article.)

$E$ was less than 4%. In addition to the elastic constants, Table 2 lists other parameters from the uniaxial tension experiments. Each of the architectures showed a peak stress followed by a modest softening, either with or without a distinct plateau region before an abrupt failure. The A1 architecture was found to have the lowest failure stress, peak/ultimate stress and strain at failure. The A2 architecture had a marginally higher (~7%) peak stress relative to A1 (0°/90° case) whereas there was a substantial increase in the

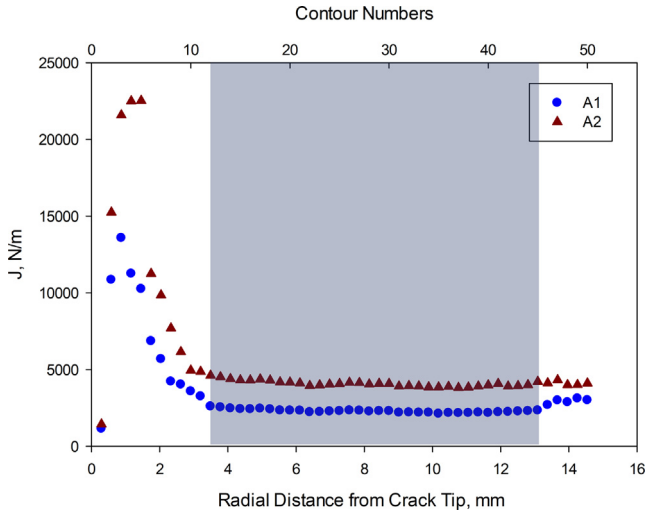


**Fig. 7.** Plots of $J$ for different contour number. Contour #12-45 corresponding to approx. 3.6–13.5 mm or $r/B$ ratio of 0.6–2.25 are used consistently for all load steps. (The reported data corresponds to the shaded part where the $J$-value varies by <5%).

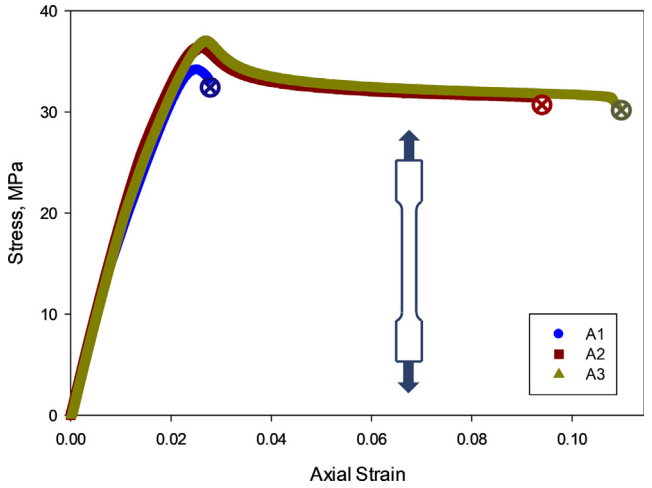


**Fig. 8.** Tensile stress-strain responses of dog-bone specimens of different print architectures. (The cross marks indicate specimen failure).

**Table 2**
Material properties obtained from tensile tests.

| Material Property | A1 | A2 | A3 |
|---|---|---|---|
| Elastic modulus (GPa) | 2.07 | 2.14 | 2.14 |
| Poisson's ratio | 0.34 | 0.34 | 0.34 |
| Failure stress (MPa) | 34.1 | 36.3 | 36.8 |
| Failure strain % | 2.8 | 9.3 | 10.9 |

Tension and Shear Responses of Reference Architectures

failure strain, by over 230%. The A3 architecture had a response similar to that of A2 [45/−45° case] in terms of its peak stress. The failure strain, however, was unexpectedly higher (by ~17%) than the A2 architecture (or, by 290% relative to A1). The increase in the strain at failure signifies higher ductility observed in the A2 and A3 architectures relative to A1.Table 3.

The stress-strain responses for the reference architectures are shown in Fig. 9. Fig. 9(a) and (b) shows the tensile stress-strain responses. The results (peak stress ~35 MPa for 0° print and ~40 MPa for the 90° print, strain-at-failure ~2.4% in both cases)

**Table 3**
Material properties of reference architectures.

| Material Property | $[0°]_n$ | $[90°]_n$ | Iosipescu Shear |
|---|---|---|---|
| Elastic/Shear modulus (GPa) | 2.10 | 2.15 | 0.8 |
| Poisson's ratio | 0.34 | 0.34 | 0.34 |
| Failure stress (MPa) | 34.8 | 39.8 | 36.1 |
| Failure strain % | 2.2 | 2.4 | 22.2 |

are nearly same as the one for the A1 (Fig. 8) architecture. The pure shear tests (Fig. 9(c)) based on Iosipescu geometry, on the other hand, show that the ultimate shear stress is ~35 MPa, close to the tensile strength of the unidirectional coupons. However, the shear strain at failure is ~23%, *ten times higher than the tensile failure strain of the 0° or 90° prints* (and the A1 architecture).

### 5.2. Quasi-static fracture tests

The load vs. load-point displacement plots for edge-cracked 3-point bend specimens for all three architectures are shown in Fig. 10. The response for the A1 architecture shows a relatively brittle response when compared to A2 and A3 counterparts. Following a linear increase up to crack initiation occurring at a peak load, a precipitous drop in load to complete fracture occurred in A1. In the A2 and the A3 architectures, on the other hand, the response was linear up to crack initiation and was significantly higher (~40%) relative to the A1 architecture. More importantly, a relatively graceful as opposed to an abrupt drop in load occurred during crack growth in A2 and A3 architectures. Furthermore, the A3 architecture showed a highly wavy load-deflection response during crack growth relative to A2.

Fig. 11 shows photographs of reassembled fractured specimens to illustrate crack propagation in all three architectures under quasi-static loading conditions. In the A1 architecture, the crack propagated self-similarly or along the direction of the pre-crack. On the other hand, the crack propagated with a staircase pattern, in one of the two 45° directions, in A2 whereas in A3, the incremental crack growth was locally along ±45° as well as 0° directions with a substantial degree of meandering and frequent jumps in between different layers along the crack path. *The latter is consistent with the wavy load-deflection response seen in* Fig. 10. As a result, the overall macroscopic crack growth direction is noticeably different from the ±45° directions observed in A2. Evidence of inelastic deformations (crazing), though not readily evident from the photographs due to the white color of ABS material used, was also observed at the crack tip and along the crack flanks indicating significantly higher crack growth resistance in the A2 and A3 architectures relative to A1. The manifestation of shear deformations along the crack path is clearly visible from the noticeable kink in crack surface striations in A3.

The gray scale photographs of surface speckles (Fig. 12(c)) recorded by the camera in the deformed state were correlated with the reference images recorded before the application of load to obtain the displacement component fields in two orthogonal directions, along ($x$) and perpendicular ($y$) to the initial crack orientation. An image analysis software, ARAMIS®, was used to perform gray scale correlation by segmenting images into 25 × 25 pixel sub-images with 5 pixels step size. The scale/magnification factor was ~30 μm/pixel for these images (It should be noted that the *displacement data are available as rectangular arrays over the ROI and at the center of each sub-image although they are displayed as contours* in these figures after post processing). The stable values from the $J$-Integral vs. contour number plot for the static experiments, averaged over contours 15–45 or 2.25 mm–7 mm or $r/B$ ratio ~0.4–1.2 (shaded region in Fig. 12), were recovered as the $J$-integral.

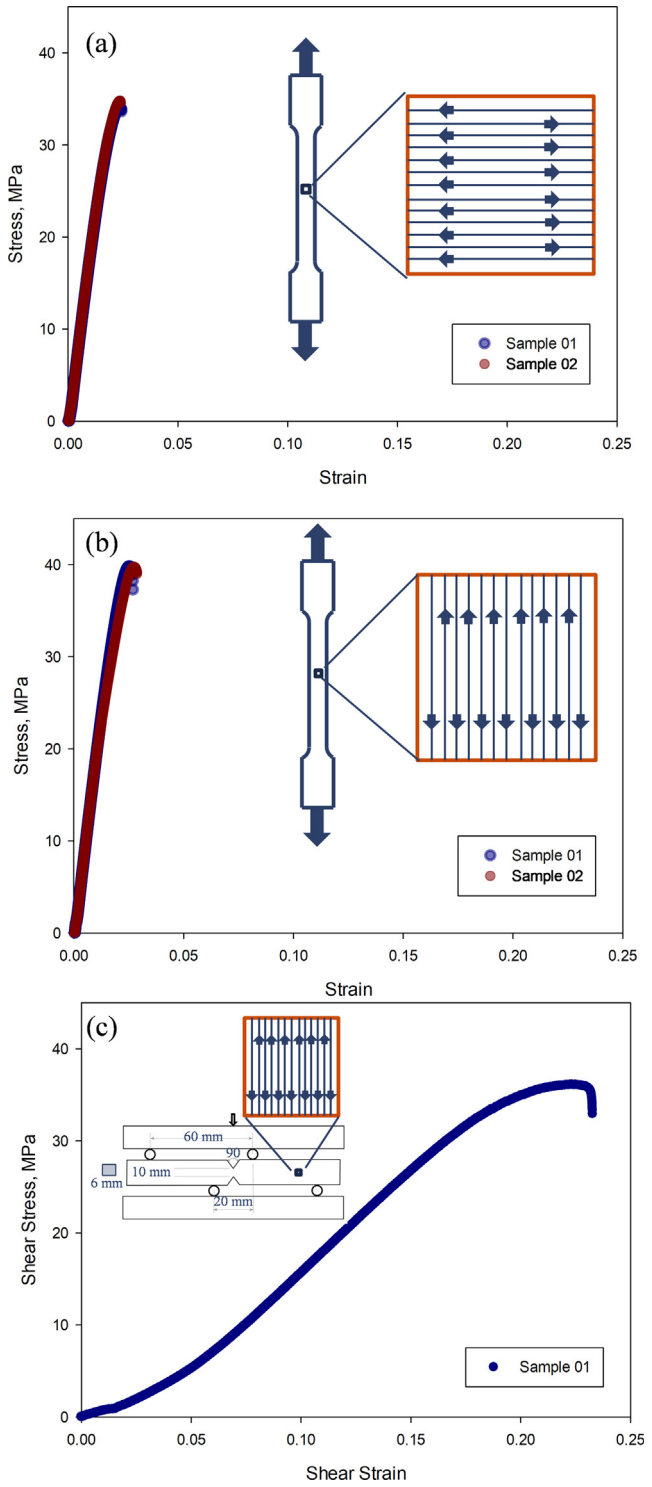


**Fig. 9.** Tensile and shear responses of unidirectionally printed reference coupons. (a) Stress-strain plots for unidirectional $[0°]_n$ tensile samples with print architecture. (b) Stress-strain plots for unidirectional $[90°]_n$ tensile samples with print architecture. (c) Shear stress- shear strain plots for $[0°]_n$ losipescu tests with specimen geometry, loading and print architecture.

Similar A2 and A3 displacement contours are not shown for conciseness.

Fig. 13 shows the crack growth resistance or *J-a* plots for all the three architectures. It can be observed from the graphs that the resistance to crack initiation, as expected, was the lowest for the A1 architecture (1850 J/m$^2$) and the same was approx. 55% higher

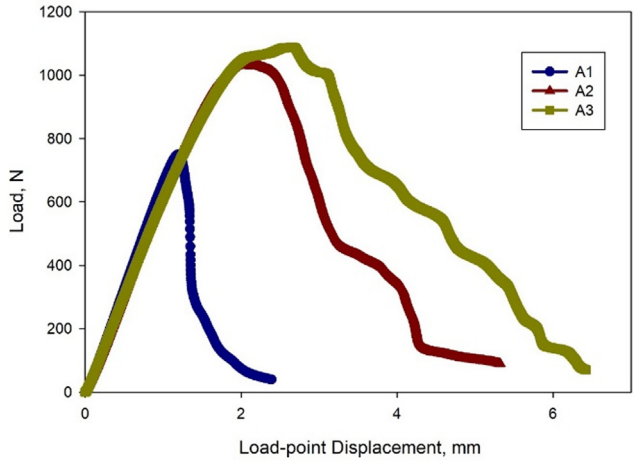


**Fig. 10.** Effect of print architecture on load vs load-point deflection for quasi-static three-point bend specimens.

for A2 (2900 J/m$^2$) and 35% higher for A3 (2500 J/m$^2$) architectures. After crack initiation, the crack growth resistance for the A1 architecture remained approx. constant or $dJ/da \sim 0$ whereas the A2 architecture showed an abrupt drop in resistance ($dJ/da < 0$ or unstable growth relative to its value at initiation) after crack initiation before building back resistance and attain $dJ/da > 0$. The A3 architecture, unlike the A2 counterpart, after crack initiation showed a steady increase in values or $dJ/da > 0$ before plateauing at ~4000 J/m$^2$, higher than that for A2 over the same amount of crack growth. The maximum values of the *J*-integral for each of these architectures in the window of observation were approx. 2250, 4000, 4450 J/m$^2$ for A1, A2, and A3, respectively.

Fig. 14 shows the *J*-integral histories from the 3-point bend specimens. For the purpose of comparing the fracture behaviors, *the time axes for each case are shifted such that t = 0 corresponds to crack initiation*. That is, the negative and positive *t* values correspond to pre- and post-initiation regimes, respectively.[2] Observations and characteristics similar to the ones made for the resistance behaviors (Fig. 13) can be made again. The architecture A1 had a quasi-brittle response whereas A2 and A3 were relatively tougher. Again, the A2 architecture showed a noticeable drop in the *J*-integral immediately after crack initiation whereas A3 had a steady increase with respect to time.

The implementation of this methodology was verified by evaluating the SIFs using the load vs. load-point plots (Fig. 10) in conjunction with the closed form solution for 3-point bend specimen configuration:

$$K_I = \frac{F \cdot S}{B \cdot W^{3/2}} \frac{3\alpha^{1/2}\left[1.99 - \alpha(1-\alpha)\{2.15 - 3.93\alpha + 2.7\alpha^2\}\right]}{2(1+2\alpha)(1-\alpha)^{3/2}},$$
$$\alpha = \frac{a}{W},\ J = \frac{K_I^2}{E} \tag{4}$$

where *F*, *S*, *W*, *B* and *a* denote applied load, beam span, height, thickness and crack length, respectively. This is shown for A1, A2 and A3 architectures in Fig. 14 where the solid symbols are the ones obtained from the DIC-FE analyses and the open symbols are from Eq. (4). Good agreement between the two is evident in each case (error percentages for A1, A2 and A3 at crack initiation are ~3.1%, ~6.2% and ~7.3% respectively). The comparison for A2 and A3 is only up to crack initiation since the closed form solution is invalid after crack initiation beyond which the crack kinks away from its initial

[2] The repeatability of *J* vs. *t* was also ensured across multiple samples and architectures. Two such examples are shown in Appendix A, Fig. A2(b).

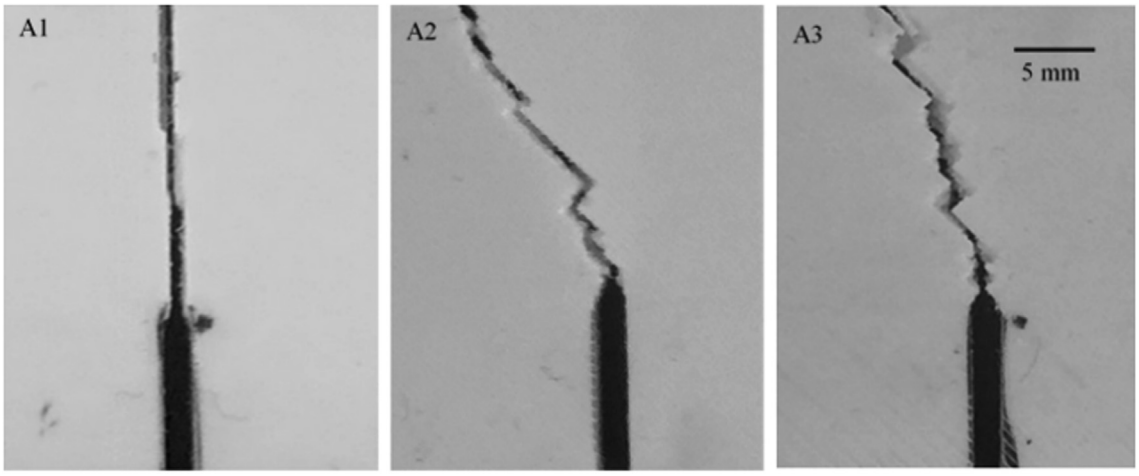


**Fig. 11.** Photographs of observed crack paths in fractured 3-point bend specimens. (The specimen A3 is flipped by 180° for consistency with A2).

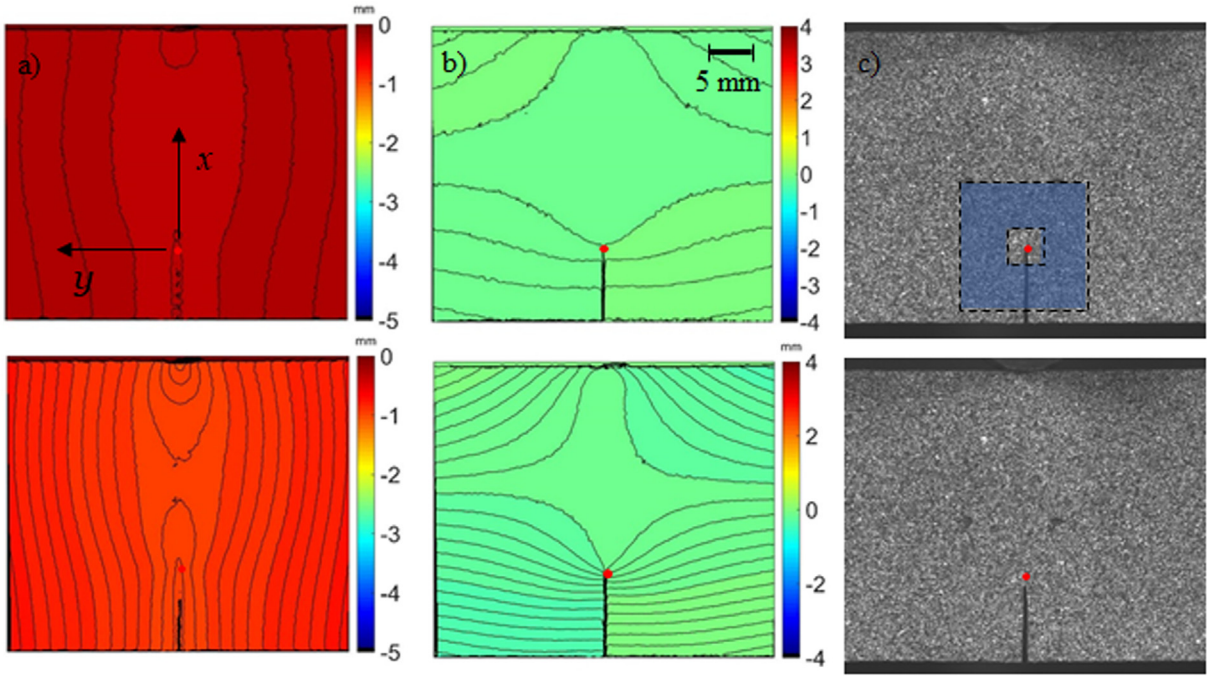


**Fig. 12.** Displacement contours of A1, with a contour interval of 20 μm, obtained through DIC (a) *x*- or *u*-field, (b) *y*-or *v*-field. (c) Speckle images corresponding to the applied load step. Red solid dots indicate the crack tip location at this time/load step. Top row corresponds to pre-crack initiation (Load = 500 N) and bottom row corresponds to post-crack initiation (Load step = 620 N) stages. (The shaded zone in the speckle image corresponds to the region where the *J*-integral is computed.) (For interpretation of the references to color in this figure legend, the reader is referred to the web version of this article.)

path whereas it is valid for the self-similar crack growth in A1.

### 5.3. Ultrasonic measurements

The results obtained from ultrasonic measurements are enumerated in Table 4. Evidently, the values of *E* are expectedly higher than the ones from uniaxial quasi-static tests due to the higher strain rates (MHz frequency) imposed by the ultrasonic transducer. More importantly, the values of these dynamic elastic constants were same in all the three directions and for all three architectures. Thus, the 3D printed architectures were *macroscopically isotropic* despite the differences in the underlying print architectures.

### 5.4. Dynamic fracture tests

As described previously, the V-notched specimens were dynamically loaded by impacting the long-bar and the resulting transient fracture event in the specimen was imaged using an ultrahigh-speed camera. To accomplish the optical mapping of deformations in the ROI, the specimens were spray painted with black/white random speckles and were photographed during the stress wave loading event using a Kirana 05 M single sensor camera[3] at a framing rate of 200,000 fps (or, inter frame rate/sampling of 5 μs). The images in the deformed state were correlated with the one in the ref-

[3] The camera is capable of recording 180, 10-bit, 924×768 pixels fixed resolution images at recording rates of up to 5 million fps.

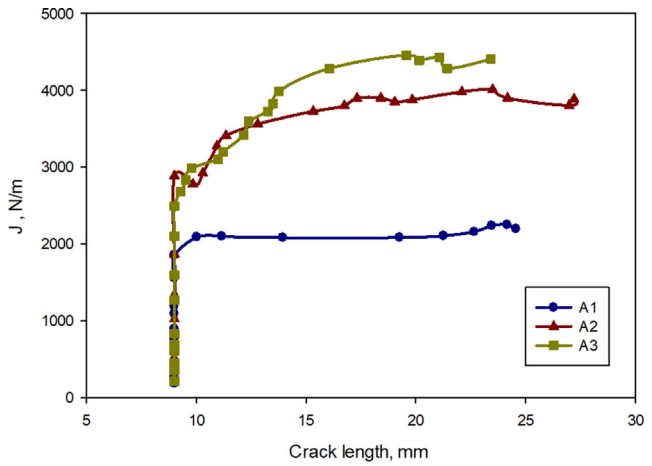


**Fig. 13.** Crack growth resistance curves for 3-point bend specimens under static condition.

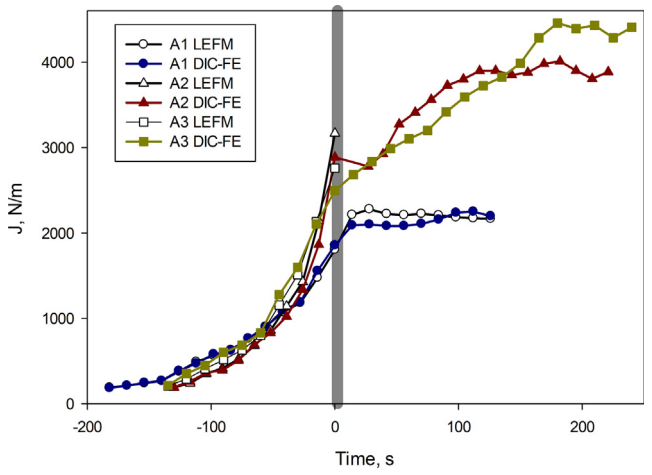


**Fig. 14.** The *J*-Integral histories for 3-point bend specimens under static conditions. Comparison between the proposed DIC-FE approach and closed form solution for A1, A2 and A3 architectures. (Negative and positive times correspond to pre- and post-crack initiation regimes.)

erence/undeformed state recorded before the start of the impact event. As in the quasi-static counterparts, the speckle image correlation was performed using ARAMIS® software. During analysis, as in quasi-static counterparts, each image was segmented into sub-images of size 25 × 25 and an overlap of 5 pixels. The scale factor was ~60 μm/pixel for all dynamic fracture experiments. Thus obtained orthogonal displacement fields were then used in conjunction with the analysis approach described earlier to extract the *J*-integral.

Figs. 15–17 show select displacement contours and speckle images for all the three print architectures A1, A2 and A3, respectively. The speckle images and displacement components $u$ and $v$ in the $x$- and $y$-directions in the pre- and post-initiation states are shown in Fig. 15 for A1. The $u$-fields are symmetric relative to the crack and the (horizontal) loading axis. The $v$-contours, on the other hand, are symmetric in shape and antisymmetric in magnitude relative to the crack. This is consistent with the mode-I deformations in the pre- and post-initiation regimes in the A1 architecture. The region, from which the *J*-Integral values are averaged, are highlighted in one of the speckle images in Fig. 15(c). The $u$- and $v$-fields along with the speckle images for the A2 architecture are shown in Fig. 16 in both the pre- and post-initiation phases. As in the A1 architecture, the $u$-contours are again symmetric whereas the $v$-contours are symmetric only shape and antisymmetric in values relative to the initial crack orientation before initiation suggesting a dominant mode-I deformation. Once the crack initiates, however, the propagation occurs in one of the two print directions, along −45° in this case. As a result, the local $u$- and $v$-deformation contours are asymmetric relative to the initial and current crack orientations and hence occurrence of mixed-mode (mode-I and -II) fracture.

The $u$- and $v$-contours and the speckle images for A3 are shown in Fig. 17. As in the A2 architecture, the displacement contours are symmetric in shape prior to crack initiation, consistent with mode-I deformations. Upon crack initiation, however, the growth occurred in this architecture along +45° as shown. That is, as in the quasi-static counterparts, the crack growth occurred in a mixed-mode fashion with locally asymmetric deformations. However, unlike the quasi-static counterpart in which a zig-zag growth of different lengths in 0° or ±45° resulted in a macroscale growth angle different from the 45°, the crack growth here occurred in a distinct 45° direction. In this architecture with an equal opportunity for the crack to propagate in the 0° or ±45° direction, the growth consistently occurred in one of the two possible 45° directions. Fig. 18 shows photographs of fractured specimens of all three architectures under dynamic conditions.

The crack length histories, obtained by inspecting the speckle images and the location where displacement contours from DIC converge, are plotted in Fig. 19. The crack growth was monotonic in all three print architectures. Also, the rates of crack growth were found to be low in all architectures. That is, they were in the range of 30–60 m/s during the observation window. These speeds are quite low (~5%) relative to the shear wave speeds (~980 m/s) (see, Table 4). *Hence, it is reasonable to adopt the J-integral evalua-*

**Table 4**
Ultrasonically measured wave speeds, density, and elastic constants for the three different print architectures in three orthogonal directions. (Density of bulk ABS based on manufacturer supplied wire stock was ~1035 Kg/m$^3$ and hence porosity based on weight difference was ~1.18%).

| Print Architecture | Axis of Measurement | Longitudinal Wave speed $C_L$ (m/s) | Shear Wave speed $C_S$ (m/s) | Density $\rho$ (Kg/m$^3$) | Poisson's Ratio $\nu$ | Elastic Modulus $E$ (GPa) |
|---|---|---|---|---|---|---|
| A1 | $x$ | 2045 | 987 | 1022 | 0.348 | 2.66 |
| | $y$ | 2041 | 986 | | 0.348 | 2.65 |
| | $z$ | 2035 | 983 | | 0.348 | 2.63 |
| A2 | $x$ | 2041 | 984 | 1022 | 0.349 | 2.67 |
| | $y$ | 2038 | 986 | | 0.347 | 2.67 |
| | $z$ | 2061 | 988 | | 0.351 | 2.69 |
| A3 | $x$ | 2060 | 988 | 1022 | 0.348 | 2.67 |
| | $y$ | 2058 | 987 | | 0.347 | 2.68 |
| | $z$ | 2061 | 985 | | 0.349 | 2.68 |

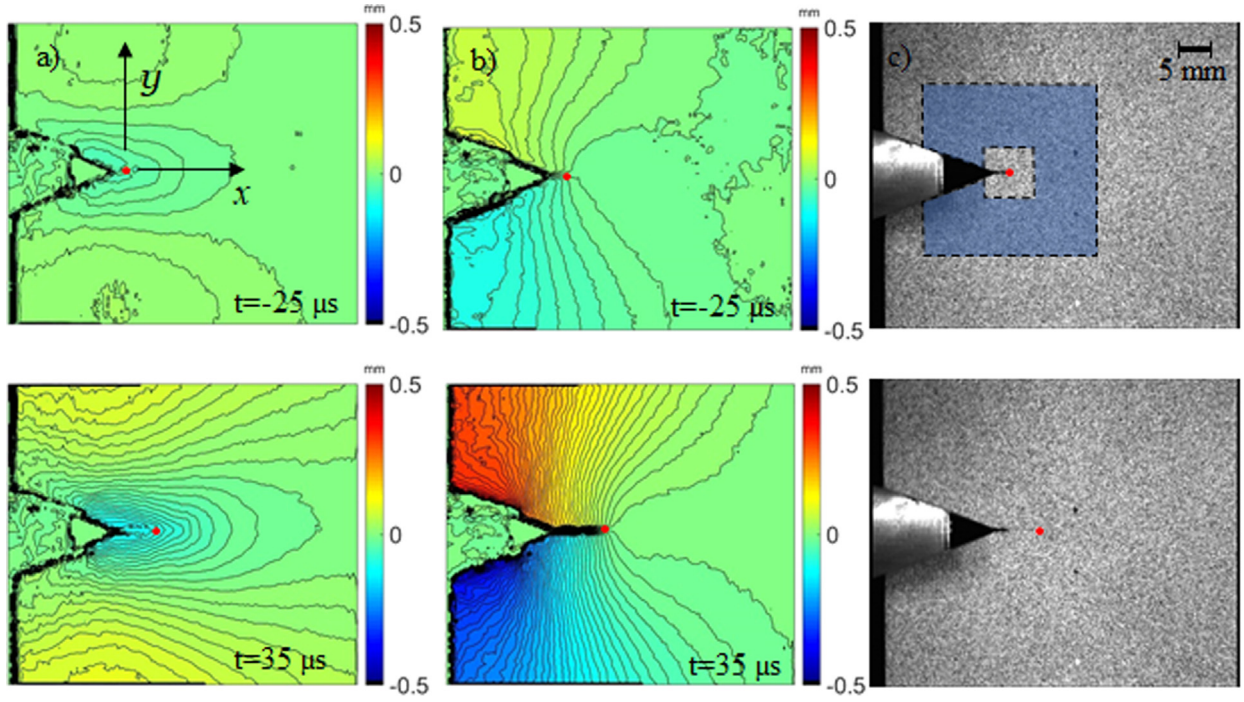


**Fig. 15.** Measured displacement contours for A1 at two time instants before and after crack initiation. Contour interval = 10 μm. (a) *x*- or *u*-field, (b) *y*-or *v*-field, (c) Speckle images corresponding to the particular time step. Red solid dots indicate the crack tip at this time step. (For interpretation of the references to color in this figure legend, the reader is referred to the web version of this article.)

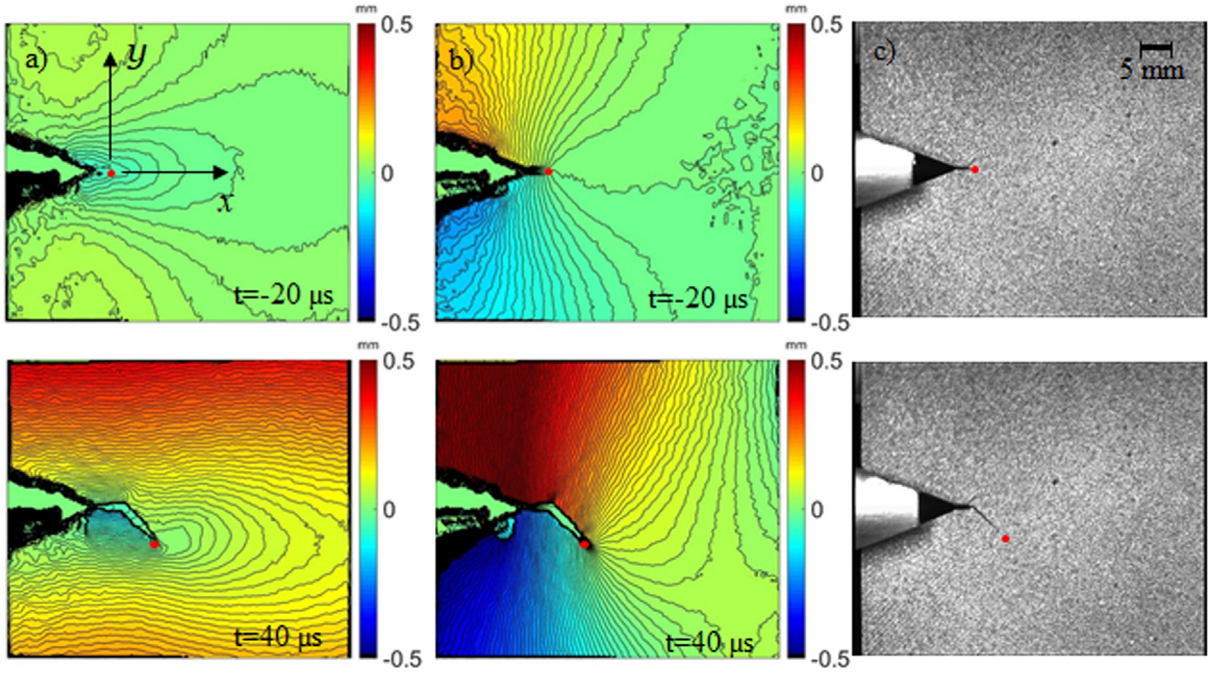


**Fig. 16.** Measured displacement contours for A2 at two time instants before and after crack initiation. Contour interval = 10 μm. (a) *x*- or *u*-field, (b) *y*-or *v*-field, (c) Speckle images corresponding to the particular time step. Red solid dots indicate the crack tip at this time step. (For interpretation of the references to color in this figure legend, the reader is referred to the web version of this article.)

*tion procedures as discussed earlier even though strictly they are not applicable to stress wave dominant conditions.*[4]

Fig. 20 shows the crack growth resistance curves for the three print architectures under dynamic loading conditions.[5] The crack

[4] For example, if the crack were propagating, say, at 30–40% of the shear wave speed of the material as it often does in brittle epoxies, acrylics and polyesters subjected to dynamic loading this approach would not be appropriate.

[5] Under dynamic conditions *J*-integral vs. velocity plot is more appropriate. However, due to very low crack speeds observed, the crack growth resistance as *J*-integral vs. crack length is reasonable and inertia effects are accounted for.

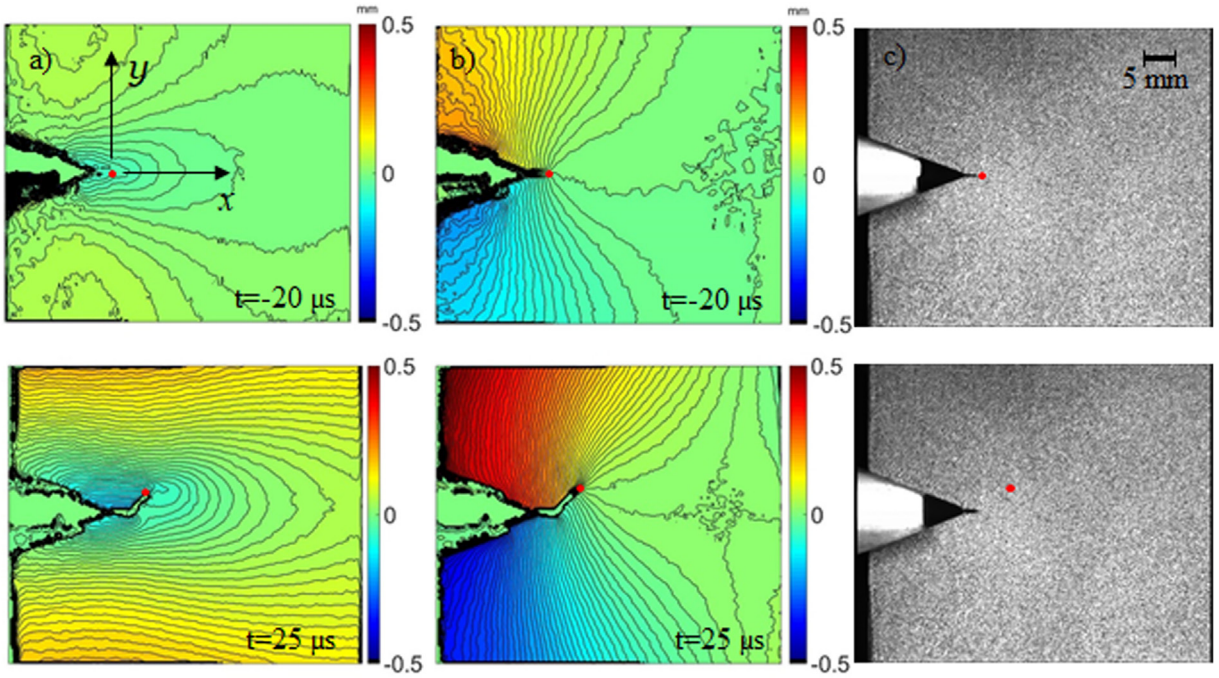


**Fig. 17.** Measured displacement contours for A3 at two time instants before and after crack initiation. Contour interval = 10 μm. (a) *x*- or *u*-field, (b) *y*-or *v*-field, (c) Speckle images corresponding to the particular time step. Red solid dots indicate the crack tip at this time step. (For interpretation of the references to color in this figure legend, the reader is referred to the web version of this article.)

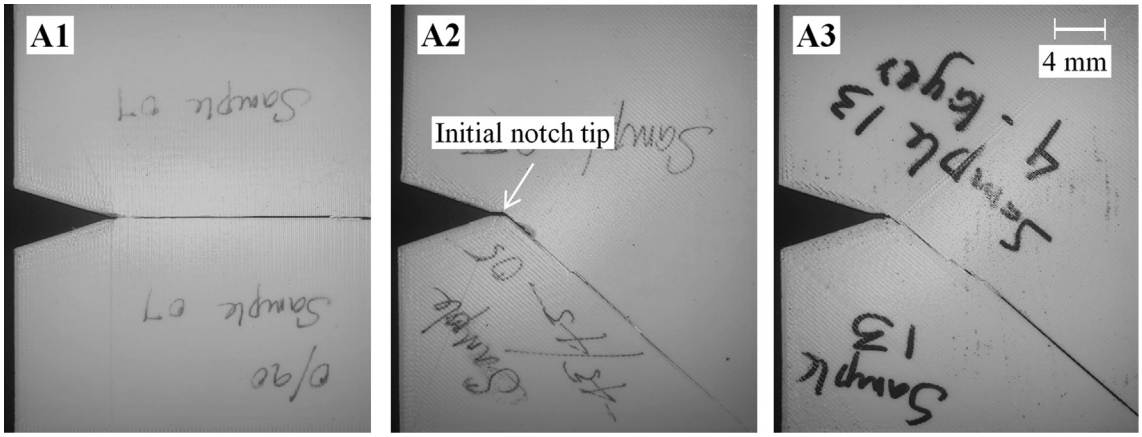


**Fig. 18.** Dynamic crack paths observed in V-notched specimens.

growth resistance in terms of the *J*-integral after crack initiation, at approx. 2300 J/m$^2$, shows an unstable crack growth event relative to the value at crack

initiation for A1 as $dJ/da < 0$. This is unlike in quasi-static counterpart (Fig. 13). In case of A2, the values of the *J*-integral drop noticeably right after crack initiation at ~4000 J/m$^2$ before building back to a steady state value of 3800 J/m$^2$. Unstable crack growth event at crack initiation is observed for this architecture. In case of A3, however, the crack growth resistance in terms of the *J*-integral initially shows $dJ/da > 0$ after initiation at ~3600 J/m$^2$ followed by increase to a nearly constant value of 4000 J/m$^2$ later in the observation window. Given these differences among the three architectures, A3 again stands out in terms of a graceful crack growth behavior relative to the other two even though A2 had a slightly higher value at crack initiation.

Fig. 21 shows the histories of the *J*-integral for all three cases under dynamic loading conditions. The resistance to crack growth continuously dropped after crack initiation (at $t = 0$) in the print architecture A1 whereas it attained higher stable values in the A2 and A3 architectures. Other aspects of crack growth behavior align well with the description provided for Fig. 20.

## 6. Discussion

It is evident from the results for the three build architectures A1, A2 and A3, the tensile responses under static and dynamic conditions show a few unexpected behaviors. The elastic properties of all three print architectures under identical testing conditions (quasi-static or dynamic/ultrasonic) did not show notable differences suggesting elastic isotropy at the macroscale. As expected, the ultrasonic measurements yielded higher elastic moduli (2.6–2.7 GPa) when compared to the quasi-static counterparts (2.05–2.15 GPa) due to the strain-rate sensitivity of the ABS. The tension tests revealed that the print architectures do not affect

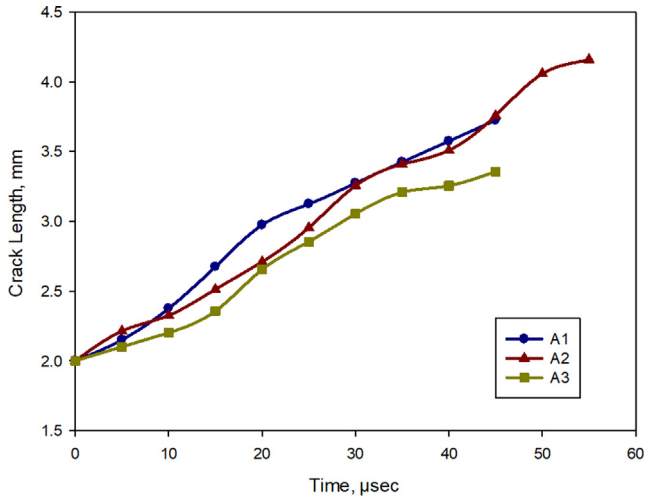


**Fig. 19.** Crack length histories for V-notched specimens subjected to dynamic loading. The crack velocities are low and in the 30–60 m/sec range; shear wave speed in this material is ~980 m/sec.

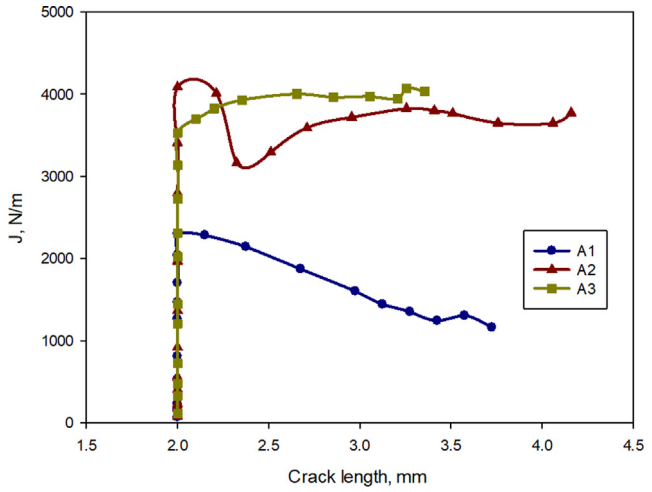


**Fig. 20.** Crack growth resistance curves for V-notched specimens under dynamic conditions.

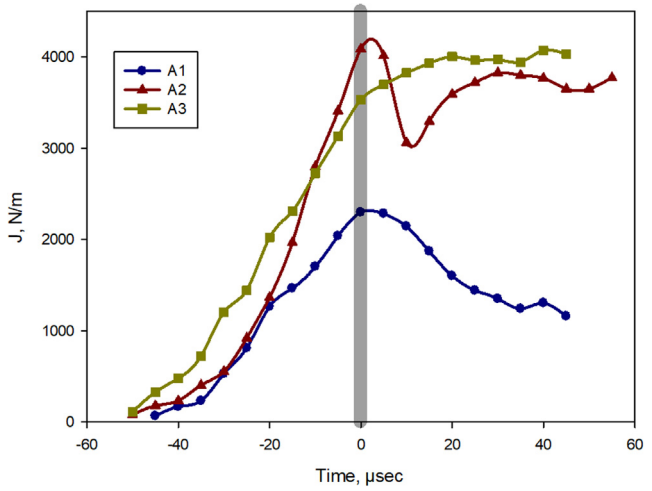


**Fig. 21.** The *J*-Integral histories for edge-notched specimens under dynamic loading condition. Negative and positive times correspond to pre- and post-crack initiation regimes.

**Table 5**
The *J*-Integral values at crack initiation under static and dynamic conditions.

| Critical Energy Release Rate $J_{cr}$, J/m$^2$ | A1 | A2 | A3 |
|---|---|---|---|
| Quasi-Static | 1850 | 2900 | 2500 |
| Dynamic | 2300 | 4000 | 3600 |

the peak/ultimate stress significantly even though the A1 architecture was found to be the weakest. However, the print architecture has a substantial influence on ductility. The strain-to-failure values were substantially different; ~2.5% for A1, ~9% for A2 and unexpectedly higher value of ~11% for A3.

From Table 5, it can be seen that A2 had the highest crack initiation toughness under both static and dynamic conditions whereas A1 was the lowest among the three architectures. In the quasi-static case, although A2 showed the highest toughness at initiation, A3 had a rather gradual/graceful failure behavior with increasing resistance to crack growth ($dJ/da > 0$). Furthermore, the measured energy release rate was the highest for A3. In the dynamic case, both A2 and A3 architectures showed a kinked crack growth along one of the 45° planes after crack initiation with A2 presenting a higher crack initiation toughness relative to A3 whereas A3 showed a stable crack growth leading to higher values of the *J*-integral relative to A2.

Despite these results, the fact that ductility of A3 is greater than that for A2 suggests additional failure mechanisms at play. The synergistic constraint between different print directions is a likely contributor to this response. This is similar to the observations of Jhaver and Tippur (Jhaver and Tippur, 2009) for a hybrid co-continuous (interpenetrating) foam material made of closed-cell polymer foam infiltrated into an aluminum open-cell foam scaffold. That is, the hybrid foam showed ~50% higher plateau stress and 35% higher energy absorption per unit mass relative to the neat syntactic foam due to synergistic constraint effects. That is, the 90° layer in the $[0/45/90/-45°]_n$ architecture mitigates the tensile stress on the 45° and −45° layers to accommodate higher shear deformations.

The tension tests can also shed light on the observed fracture characteristics of all three build architectures. The low crack initiation toughness followed by crack growth at a stable value of the *J*-integral for A1 is consistent with the low ductility observed in the $[0°]_n$ and $[90°]_n$ coupons (Fig. 9). Relatively high crack initiation toughness followed by unstable crack growth along one of the two 45° directions in A2 is also consistent with the higher shear strain-at-failure in the Iosipescu sample as the crack kinks into a 45° plane and endures combined tensile and shear deformations. The meandering of the crack between +45° and −45° planes also suggests the possibility of a jagged, instead of a straight, crack front with smeared deformations relative to the A1 sample. These failure mechanisms are further amplified in case of A3 with the crack front having opportunities for ±45° as well as 0° growth along the weaker planes between the individual strings of the print and a macroscale growth in a direction not necessarily along ±45°. Under dynamic loading conditions, the above failure mechanisms cannot manifest fully as in quasi-static conditions due to temporal constraints. For example, both A2 and A3 architectures produce fracture along a dominant 45° path with a somewhat higher degree of meandering of the crack in the latter relative to the former. Additionally, an unstable crack growth behavior in terms of the rate of change of the *J*-integral was rather pronounced in both A1 and A2 architectures. Furthermore, given equal opportunities for the crack to grow in the 0° or 45° directions, the crack growth in a 45° path confirms lower failure strain in the normal direction relative to failure strain in shear.

## 7. Conclusions

The tensile and fracture behaviors of additively printed ABS were studied in order to understand the role of print/build architecture and the loading rate on additively fabricated parts. The optical method of 2D-DIC was employed to map crack tip deformations in the whole field. The dynamic experiments were performed successfully by utilizing DIC in conjunction with ultrahigh-speed photography and a modified Hopkinson pressure bar loading apparatus. Even though all the prints showed elastic isotropy at the macroscale, distinctly different failure loads, fracture surface morphologies, and crack growth patterns were evident in the three architectures, A1 or $[0°/90°]_n$, A2 or $[45°/-45°]_n$ and A3 or $[0°/45°/90°/-45°]_n$, considered. A method of importing optically measured displacement fields into corresponding finite element discretization as full-field surface boundary conditions to extract the *J*-integral using in-built domain integral algorithms was adopted.

The tension tests showed that ductility and mechanical toughness were higher for the A2 and A3 architectures when compared to the A1 counterpart. It was evident from the failed cross-sections that the higher failure strains were due to shear deformations. The A3 architecture, however, showed a surprisingly higher ductility relative to A2 and was ascribed to mechanical constraint between layers.

The quasi-static fracture results showed that the fracture toughness of A2 and A3 architectures were higher than the A1 counterpart. The results also demonstrated that ductility and energy absorption during crack growth was higher for the above said architectures. In addition, different failures modes and crack propagation paths were observed in these cases. The A2 architecture was found to have the highest crack initiation toughness whereas A3 counterpart had a marginally lower value but higher crack growth resistance. The crack grew in a staircase pattern in A2 along ±45° planes whereas the same was much more tortuous in A3 due to crack growth along ±45° as well as 0° planes. The mechanics of these distinctly different failure behaviors could be explained in terms of tension and shear tests performed on tensile and shear specimens with unidirectional print architectures. The high ductility seen in pure shear tests explain the failure behaviors seen in the fracture specimens.

The dynamic results were consistent with the quasi-static counterparts in terms of crack initiation toughness and crack growth resistance behaviors. That is, A3 architecture outperformed A2 and A1, respectively, during crack growth. However, unlike the quasi-static fracture results, the staircase pattern of crack path was not prominent in the dynamic counterparts of the A3 architecture due to temporal limitations for the failure modes to manifest fully.

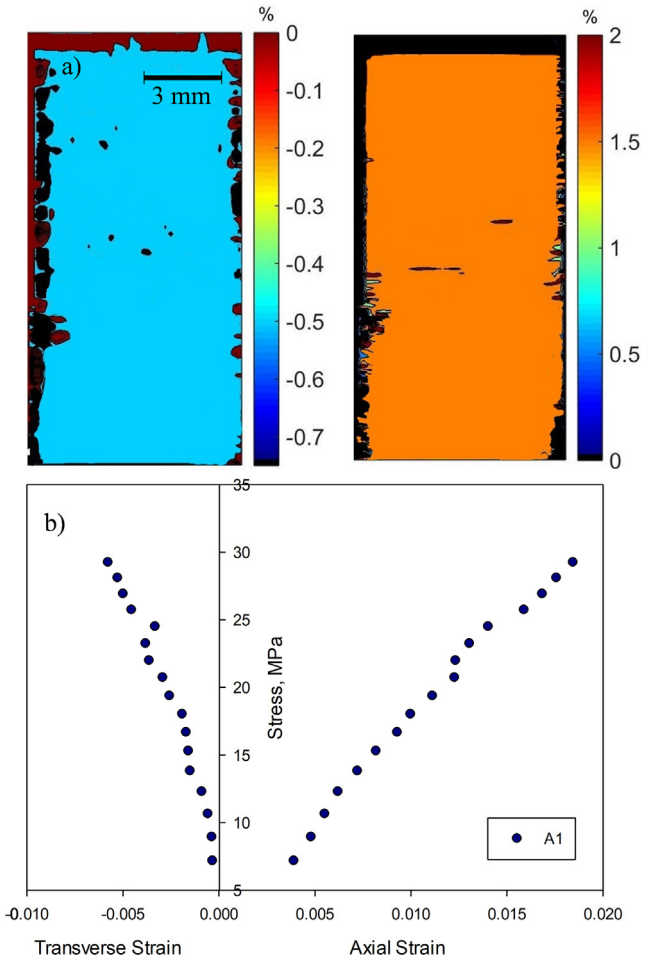


**Fig. A1.** Uniaxial tension test results from DIC: (a) $\varepsilon_{xx}$ and or $\varepsilon_{yy}$ strain fields of A1 architecture (b) Stress vs. axial and transverse strain plots of A1 architecture used to calculate elastic modulus and Poisson's ratio.

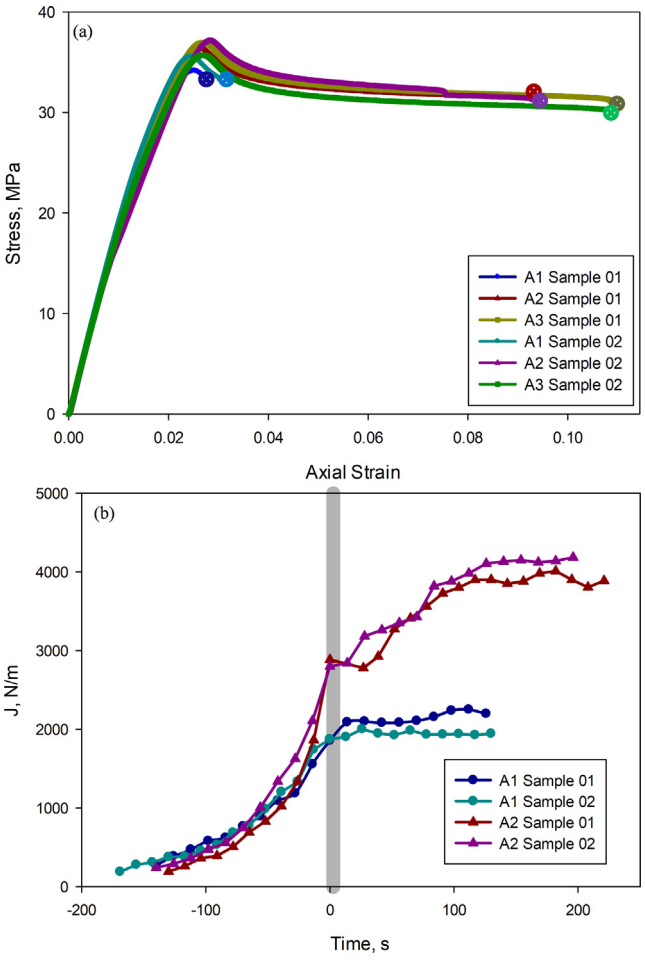


**Fig. A2.** (a) Repeatability for tensile stress–strain responses for all three architectures. (b) Repeatability for *J* vs Time plots for the A1 and A2 architectures.

## Declaration of Competing Interest

The authors declare that they have no known competing financial interests or personal relationships that could have appeared to influence the work reported in this paper.

## Acknowledgements

The authors would like to acknowledge the support of 2018 PAIR Tier III grant (PI: Dr. Nima Shamsaei) from Auburn University to carry out this research.

## Appendix-A

Test Details and Experimental Repeatability: The spray painted random speckles were recorded to measure both longitudinal and lateral strains in the gage section of the specimen using DIC and enable evaluation of the elastic constants $E$ and Poisson's ratio ν for each of the architectures. A pair of representative displacement fields from the uniaxial test on A1 architecture is shown in Fig. A1 (a). It also shows stress vs. longitudinal and lateral strain plots in the linear range for this architecture (Fig. A1(b)).

Repeatability of tension and fracture tests were ensured by studying multiple tension and fracture samples. Some examples are included in Fig. A2. Fig. A2(a) shows two repeatable tension tests for all three architectures - A1, A2 and A3. The extracted values of the $J$-integral for two A1 and two A2 samples over pre- and post-crack initiation phases are shown in Fig. A2(b). Again, in these experiments, crack initiation and growth events, the $J$-integral histories were rather repeatable.

## References

Ahn, S., Montero, M., Odell, D., Roundy, S., Wright, P., 2002. Anisotropic material properties of fused deposition modeling ABS. Rapid Prototyping J. 8 (4), 248–257.

Aliheidari, N., Tripuraneni, R., Ameli, A., Nadimpalli, S., 2017. Fracture resistance measurement of fused deposition modeling 3D printed polymers. Polym. Test. 60, 94–101.

Al-Maharma, A., Sendur, P., 2018. Review of the main factors controlling the fracture toughness and impact strength properties of natural composites. Mater. Res. Express 6, (2) 022001.

Barhli, S., Mostafavi, M., Cinar, A., Hollis, D., et al., 2017. J-integral calculation by finite element processing of measured full-field surface displacements. Exp. Mech. 57 (6), 997–1009.

Becker, T., Marrow, T., Tait, R., 2011. Damage, crack growth and fracture characteristics of nuclear grade graphite using the Double Torsion technique. J. Nucl. Mater. 414 (1), 32–43.

Becker, T.H., Mostafavi, M., Tait, R.B., Marrow, T.J., 2012. An approach to calculate the J-integral by digital image correlation displacement field measurement. Fatigue Fract. Eng. Mater. Struct. 35 (10), 971–984.

Bedsole, R.W., Bogert, P.B., Tippur, H.V., 2015. An experimental investigation of interlaminar and intralaminar dynamic fracture of CFRPs: effect of matrix modification using carbon nanotubes. Compos. Struct. 132, 1043–1055.

Bourell, D., Rosen, D., Leu, M., 2014. The Roadmap for Additive Manufacturing and Its Impact. Print. Additive Manuf. 1 (1), 6–9.

Cherepanov, G., 1967. Crack propagation in continuous media. J. Appl. Math. Mech. 31 (3), 503–512.

Dizon, J., Espera, A., Chen, Q., Advincula, R., 2018. Mechanical characterization of 3D-printed polymers. Addit. Manuf. 20, 44–67.

Gardan, J., Makke, A., Recho, N., 2016. A method to improve the fracture toughness using 3D printing by extrusion deposition. Procedia Struct. Integrity 2, 144–151.

Hareesh, T., Chiang, F., 1988. Integrated experimental-finite element approach for studying elasto-plastic crack-tip fields. Eng. Fract. Mech. 31 (3), 451–461. https://doi.org/10.1016/0013-7944(88)90087-2.

Hart, K.R., Wetzel, E.D., 2017. Fracture behavior of additively manufactured acrylonitrile butadiene styrene (ABS) materials. Eng. Fract. Mech. 177, 1–13.

Jajam, K., Tippur, H., 2011. An experimental investigation of dynamic crack growth past a stiff inclusion. Eng. Fract. Mech. 78 (6), 1289–1305.

Jhaver, R., Tippur, H., 2009. Processing, compression response and finite element modeling of syntactic foam based interpenetrating phase composite (IPC). Mater. Sci. Eng., A 499 (1–2), 507–517.

Jia, Z., Wang, L., 2019. 3D printing of biomimetic composites with improved fracture toughness. Acta Mater. 173, 61–73.

Kirugulige, M.S., Tippur, H.V., Denney, T.S., 2007. Measurement of transient deformations using digital image correlation method and high-speed photography: application to dynamic fracture. Appl. Opt. 46 (22), 5083.

Kirugulige, M.S., Tippur, H.V., 2009. Measurement of fracture parameters for a mixed-mode crack driven by stress waves using image correlation technique and high-speed digital photography. Strain 45, 108–122.

Lanzillotti, P., Gardan, J., Makke, A., Recho, N., 2019. Enhancement of fracture toughness under mixed mode loading of ABS specimens produced by 3D printing. Rapid Prototyping J. 25 (4), 679–689.

Lee, W.-S., Shen, H.-C., 2004. Comparisons of deformation and fracture behaviour of PC/ABS blend and ABS copolymer under dynamic shear loading. Mater. Sci. Technol. 20 (1), 8–15.

Lee, D., Tippur, H.V., Kirugulige, M., Bogert, Philip, 2009. Experimental study of dynamic crack growth in unidirectional graphite/epoxy composites using digital image correlation method and high-speed photography. J. Compos. Mater. 43 (9), 2081–2108.

Mclouth, T.D., Severino, J.V., Adams, P.M., Patel, D.N., et al., 2017. The impact of print orientation and raster pattern on fracture toughness in additively manufactured ABS. Addit. Manuf. 18, 103–109.

Mohamed, O., Masood, S., Bhowmik, J., 2015. Optimization of fused deposition modeling process parameters: a review of current research and future prospects. Adv. Manuf. 3 (1), 42–53.

Mulliken, A., Boyce, M., 2006. Mechanics of the rate-dependent elastic–plastic deformation of glassy polymers from low to high strain rates. Int. J. Solids Struct. 43 (5), 1331–1356.

O'Dowd, N.P., Shih, C.F., Stout, M.G., 1992. Test geometries for measuring interfacial fracture toughness. Int. J. Solids Struct. 29 (5), 571–589.

Pan, B., Qian, K., Xie, H., Asundi, A., 2009. Two-dimensional digital image correlation for in-plane displacement and strain measurement: a review. Meas. Sci. Technol. 20, (6) 062001.

Papon, E., Haque, A., 2019. Fracture toughness of additively manufactured carbon fiber reinforced composites. Addit. Manuf. 26, 41–52.

Peterson, A, Bolling, et al. (2015). Dynamic Behavior of Acrylonitrile Butadiene Styrene Under Impact Loads. V009T12A001. 10.1115/IMECE2015-53035. 53035.

Pitti, R.M., Badulescu, C., Grédiac, M., 2014. Characterization of a cracked specimen with full-field measurements: direct determination of the crack tip and energy release rate calculation. Int. J. Fract. 187 (1), 109–121.

Poh, P., Chhaya, M., Wunner, F., De-Juan-Pardo, E.M., et al., 2016. Polylactides in additive biomanufacturing. Adv. Drug Deliv. Rev. 107, 228–246.

Rabbi, M., Chalivendra, V., Li, D., 2019. A novel approach to increase dynamic fracture toughness of additively manufactured polymer. Exp. Mech. 59 (6), 899–911.

Rice, J.R., 1968. A path independent integral and the approximate analysis of strain concentration by notches and cracks. J. Appl. Mech. 35 (2), 379–386.

Riddick, J.C., Haile, M.A., Wahlde, R.V., Cole, D.P., Bamiduro, O., Johnson, T.E., 2016. Fractographic analysis of tensile failure of acrylonitrile-butadiene-styrene fabricated by fused deposition modeling. Addit. Manuf. 11, 49–59.

Samykano, M., Selvamani, S.K., Kadirgama, K., Ngui, W.K., et al., 2019. Mechanical property of FDM printed ABS: influence of printing parameters. Int. J. Adv. Manuf. Technol. 102 (9–12), 2779–2796.

Siviour, C.R., Jordan, J.L., 2016. High strain rate mechanics of polymers: a review. J. Dynamic Behavior Mater. 2, 15–32.

Standard Terminology for Additive Manufacturing Technologies. (2012). ASTM International Designation: F2792-12a.

Vairis, A., Petousis, M., Vidakis, N., Savvakis, K., 2016. On the strain rate sensitivity of ABS and ABS plus fused deposition modeling parts. J. Mater. Eng. Perform. 25 (9), 3558–3565.

Van de Velde, K., Kiekens, P., 2002. Biopolymers: overview of several properties and consequences on their applications. Polym. Test. 21 (4), 433–442.

Walley, S.M., Field, J.E., 1994. Strain rate sensitivity of polymers in compression from low to high rates. DYMAT J. 1, 211–227.

Yoneyama, S., Ogawa, T., Kobayashi, Y., 2007. Evaluating mixed-mode stress intensity factors from full-field displacement fields obtained by optical methods. Eng. Fract. Mech. 74 (9), 1399–1412.

Young, D., Wetmore, N., Czabaj, M., 2018. Interlayer fracture toughness of additively manufactured unreinforced and carbon-fiber-reinforced acrylonitrile butadiene styrene. Addit. Manuf. 22, 508–515.